# Supplementary Material: High resolution wind-tunnel investigation about the effect of street trees on pollutant concentration and street canyon ventilation

Sofia Fellini[a,*], Massimo Marro[a], Annika Vittoria Del Ponte[b], Marilina Barulli[b], Lionel Soulhac[a], Luca Ridolfi[b], Pietro Salizzoni[a]

[a] *Univ Lyon, INSA Lyon, CNRS, Ecole Centrale de Lyon, Univ Claude Bernard Lyon 1, LMFA, UMR5509, 69621, Villeurbanne France*
[b] *Department of Environmental, Land, and Infrastructure Engineering, Politecnico di Torino, Corso Duca degli Abruzzi 24, 10129 Turin, Italy*

## S1. Characterization of the logarithmic profile for the mean velocity above the urban canopy

The vertical velocity profile in the wind tunnel is influenced by the presence of the obstacles in its lower part, i.e. the roughness sublayer. Above this region, the mean velocity profile is usually modelled by the logarithmic law:

$$\frac{U}{u^*} = \frac{1}{\kappa} \ln \frac{z-d}{z_0}, \tag{1}$$

where $\kappa = 0.4$ is the Von Kármán constant, $z_0$ is the aerodynamic roughness length, $d$ is the zero-plane displacement, and $u_*$ is the friction velocity. In the literature, several techniques have been developed to determine the values of these parameters (Raupach et al., 2006). Here, we compare the results from two different methods.

In the first method (Salizzoni et al., 2008), the values of the three parameters were selected so as to minimize the sum of the square difference between the logarithmic velocity profile and the measurements (Fig. S1.b). The logarithmic profile only applies to a fraction of the full velocity profile. Moreover, in urban boundary layers, the inertial sublayer is squeezed by the roughness sublayer that,

*Corresponding author
*Email address:* sofia.fellini@ec-lyon.fr (Pietro Salizzoni)

as seen above, extends beyond the height of the obstacles. This fact makes the delimitation of the inertial zone even more complex than in boundary layers developing over smooth or slightly rough walls. For these reasons, we explored different extensions of the fitted region in the range $0.15 < z/\delta < 0.4$. The resulting parameters were estimated equal to $u_*/U_\infty = 0.051$, $z_0/\delta = 9 \times 10^{-4}$, and $d/\delta = 0.085$.

In the second method, the friction velocity $u_*$ was inferred from the vertical profile of the Reynolds shear stress $-\overline{u'w'}$, where $u'$ and $w'$ are the turbulent fluctuations of the horizontal and vertical velocity, respectively. Except for a thin layer close to the wall, where viscous effects are dominant, the total stress ($\tau = \rho_a u_*^2$) in the surface layer almost matches with the Reynolds stress, which is observed to be almost constant in this layer. Thus, we can write: $\tau = \rho_a u_*^2 = -\rho_a \overline{u'w'}$. Following this method, we have analysed the vertical profile of the Reynolds stresses (Fig. S1.c) which was obtained as a spatial average over the four horizontal positions reported in the inset of Fig. S1.a. A constant-stress region (red filled markers) was detected for $0.14 < z/\delta < 0.36$ and the corresponding $u_*/U_\infty$ was evaluated equal to 0.046. We note that varying the extension of the considered constant-stress region in the range $H/\delta < z/\delta < 0.4$, slight changes (of the order of 4 %) in the estimated value of $u_*/U_\infty$ are found. The normalized aerodynamic roughness ($z_0/\delta = 5 \times 10^{-4}$) and non-dimensional zero-plane displacement ($d/\delta = 0.1$) were then estimated through a linear regression of the logarithmic law in the semi-log domain.

The results from the two methods are slightly different but in line with previous experimental studies (Rafailidis, 1997; Salizzoni et al., 2008; Garbero et al., 2010). However, since the Reynolds stresses measured by a 45° X-probe HWA are usually underestimated by about 10%-20% (Tutu and Chevray, 1975; Cheng et al., 2007; Marro et al., 2020), we adopt the parameters estimated by minimum mean square error, namely (in non-normalized values) $u^* = 0.29$ m/s, $d = 0.09$ m, $z_0 = 1 \times 10^{-3}$ m.

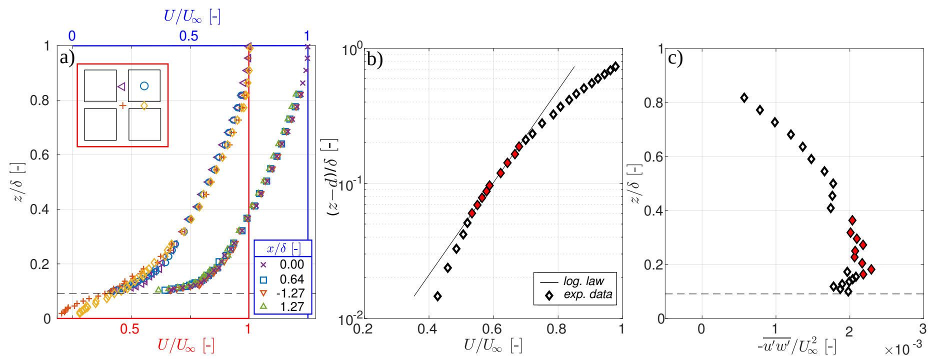


Figure S1: a) Mean velocity at 4 different position in a space periodic unit (red bottom $x$-axis) and at 4 different distances along the streamwise direction of the wind tunnel (blue top $x$-axis). For the two groups of profiles, a vertical line corresponding the $U/U_\infty = 1$ is reported. The horizontal dashed line corresponds to the canyon roof level ($H$). b) Mean velocity obtained as average over four different positions. The line represents the logarithmic law with $u_*/U_\infty = 0.051$, $z_0/\delta = 9 \times 10^{-4}$, and $d/\delta = 0.085$. The full symbols indicate the region where the logarithmic law applies. c) Reynolds stresses $-\overline{u'w'}$. The full symbols indicate the constant-stress region.

## S2. Measurement grid for the concentration field

The concentration field inside the street canyon was measured on a high-refined measurement grid with around 1000 sampling points for each configuration of tree density. The grid was not exactly the same for the different configurations due to the presence of trees. In Fig. S2, we report the measurement grid over a single horizontal plane for the different configurations. The same grid was repeated at different heights, namely $z/H = 0.2$, 0.4, 0.6, 0.8, and 1.

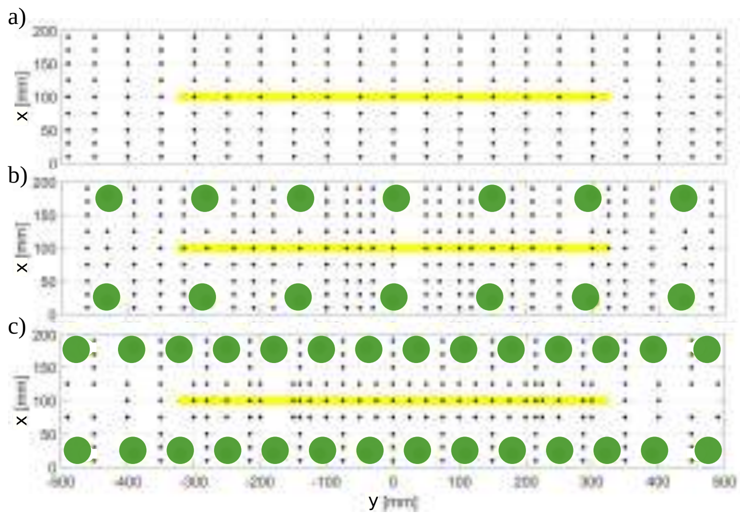


Figure S2: Sketch of the street canyon with the three different configurations of tree density: a) *Zero*, b) *Half*, and c) *Full*. The measurement grid is also shown for one of the five horizontal planes at fixed z.

## S3. Concentration field inside the canyon

In addition to the measurements already shown in the main text (Section 3.1), we report here the concentration field over all the measured vertical planes ($yz$-planes) inside the canyon. Figs. S3-S5 show the concentration field for the *Zero*, *Half*, and *Full* configurations, respectively.

Finally, we report in Fig. S6 the concentration field on the horizontal plane placed at $z/H = 0.2$. This is the minimum measurement height in the experiment and corresponds to approximately 4 m in real scale. Although this elevation is greater than the pedestrian level, which is usually considered to be 1.5 m, the concentration field at this height can still give some insights about the exposure of citizens in the street. The figure shows how, in the case without trees (panel a), the concentration at the downwind wall is roughly 3 times lower than the one at the upwind wall, while in presence of trees this difference increases up to 8 times at $y/H \approx$ -2 and 2. Despite the presence of concentration peaks at the upwind wall, we note that in the vegetated canyon, the

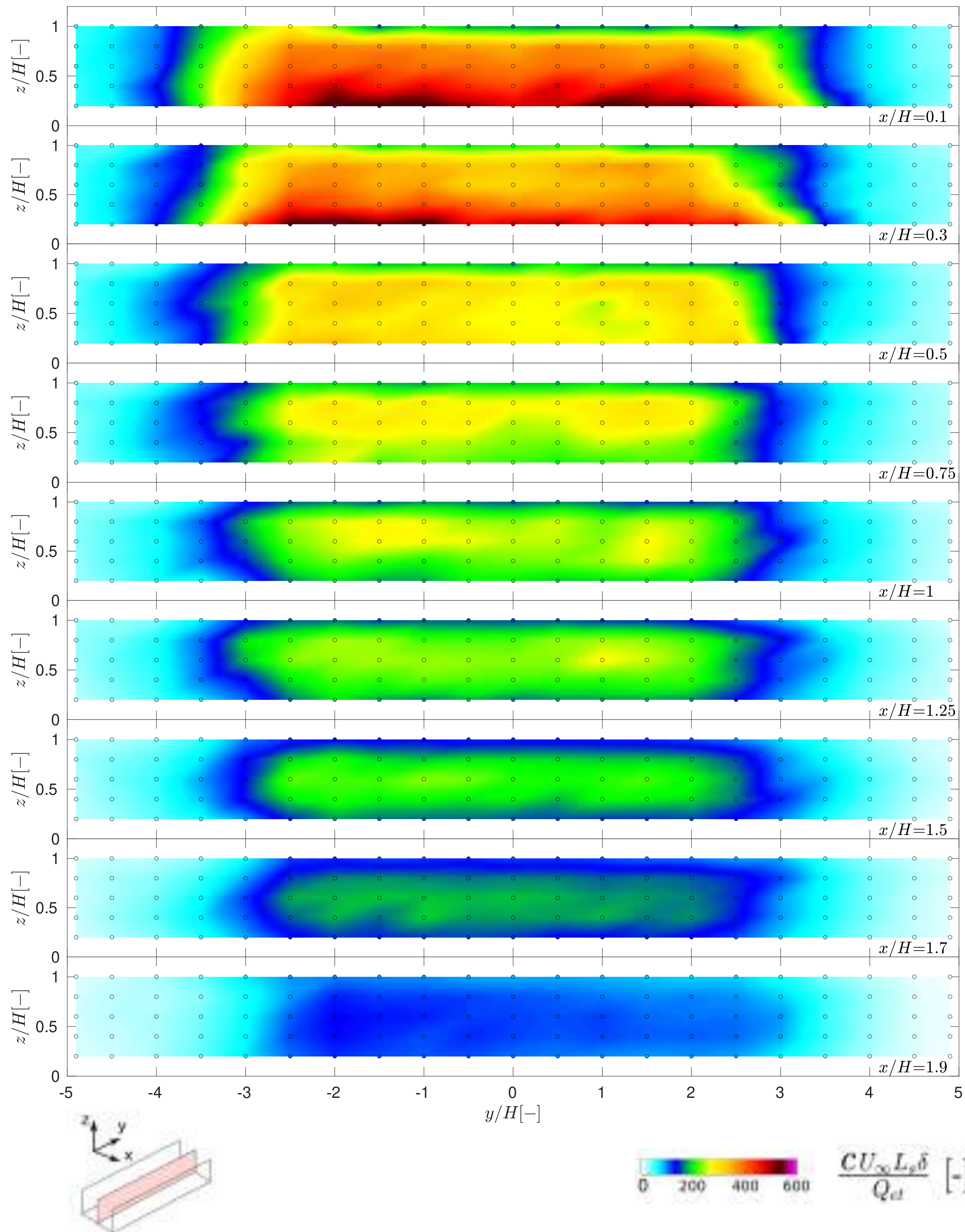


Figure S3: Configuration *Zero*. Mean concentration of the passive scalar on vertical sections at different $x$ positions. Measurement points are reported as circles coloured according to the measured value.

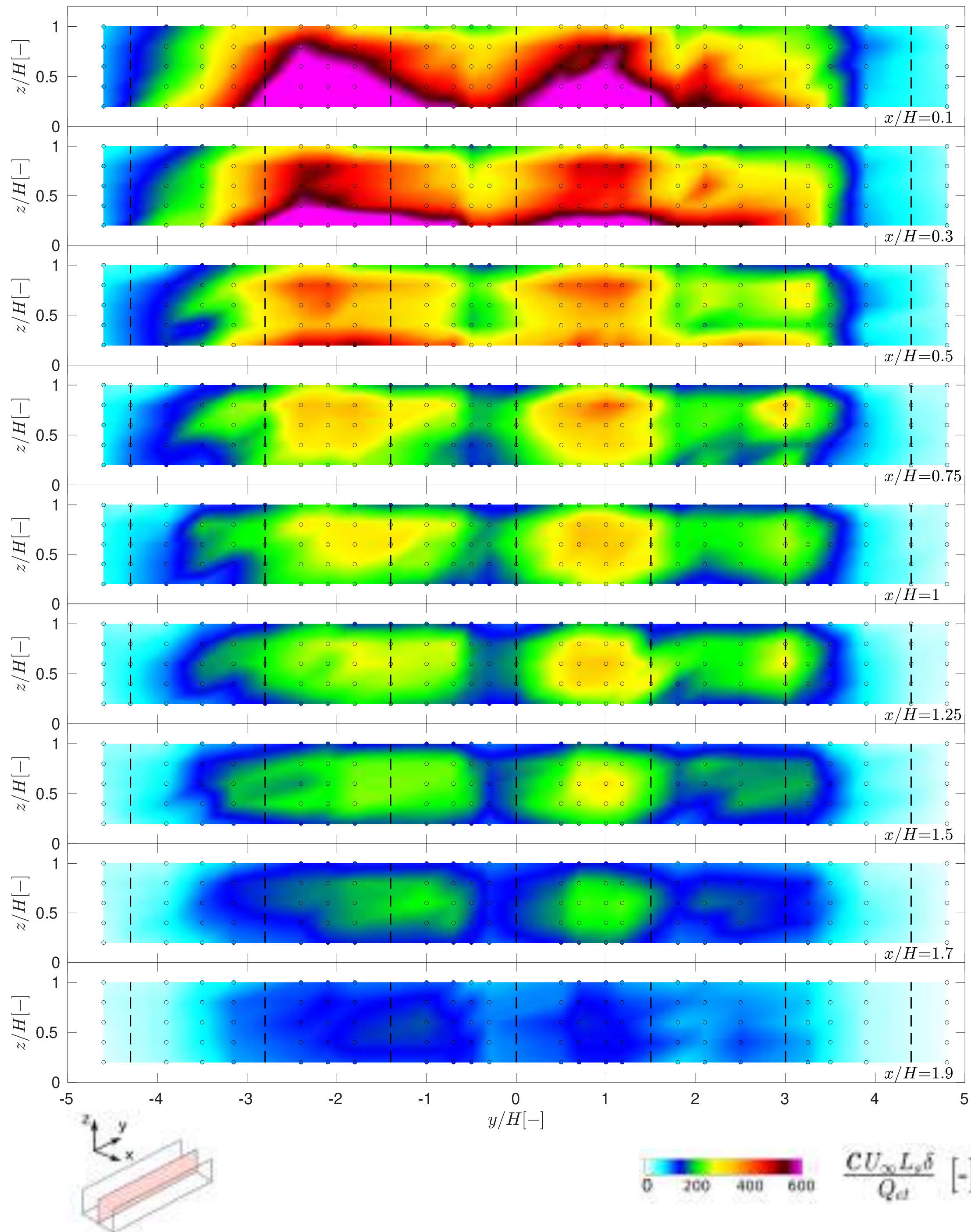

Figure S4: Configuration *Half*. Mean concentration of the passive scalar on vertical sections at different $x$ positions. The position of trees is represented by dashed lines. Measurement points are reported as circles coloured according to the measured value.

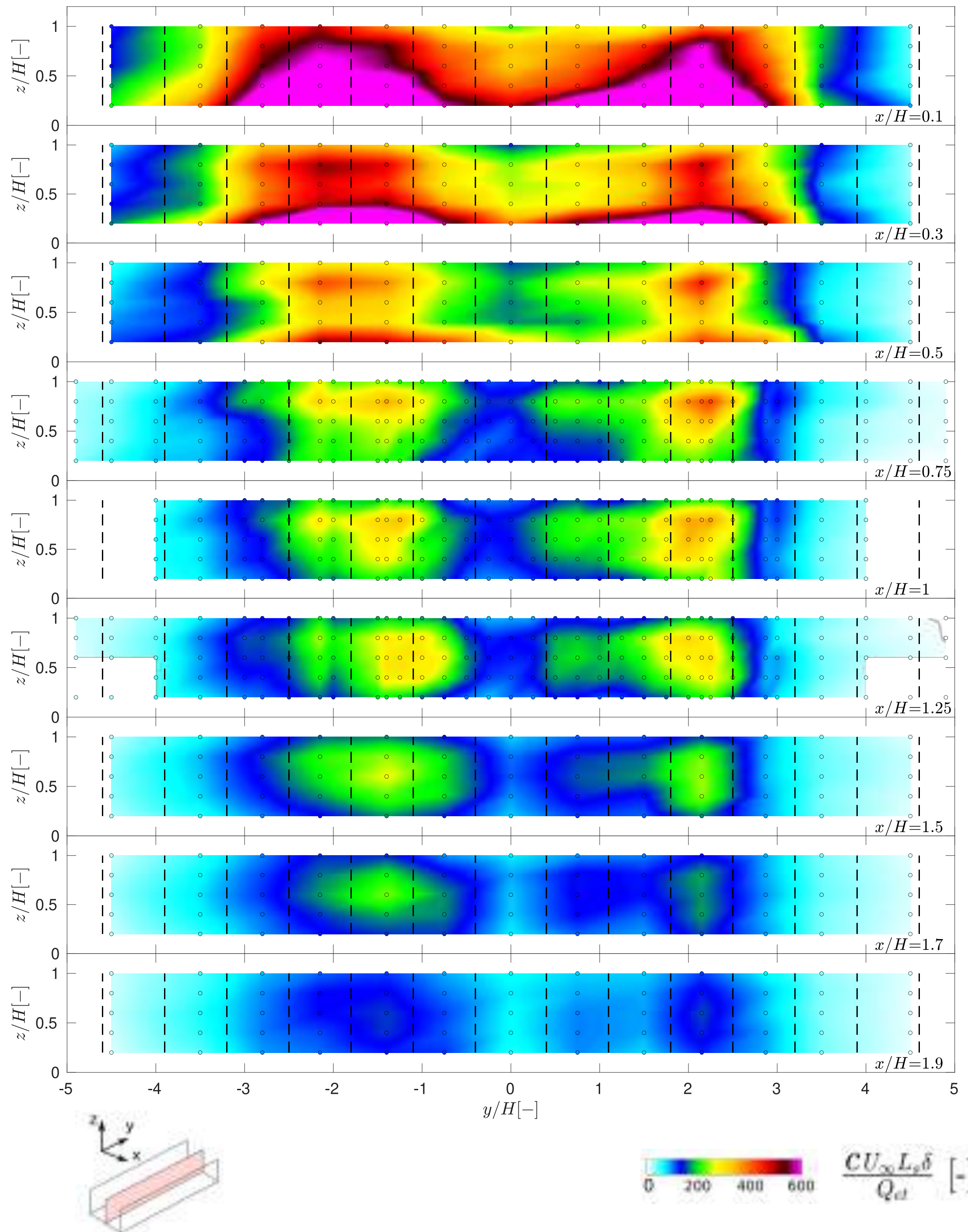


Figure S5: Configuration *Full*. Mean concentration of the passive scalar on vertical sections at different $x$ positions. The position of trees is represented by dashed lines. Measurement points are reported as circles coloured according to the measured value.

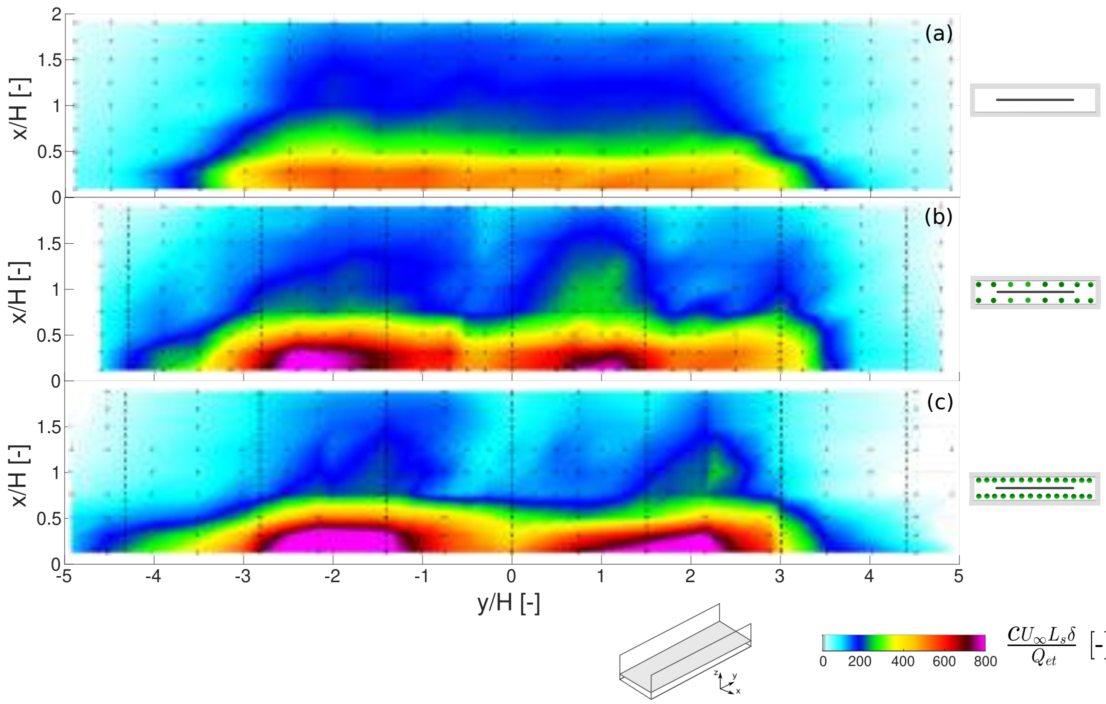


Figure S6: Mean concentration of the passive scalar on the horizontal section at $z/H$=0.2. *Zero* (a and d), *Half* (b and e) and *Full* (c and f) configurations are shown. The position of trees is represented by dashed lines. Measurement points are reported as circles colored according to the measured value.

concentrations at the downwind wall are lower than in the empty canyon.

## References

Cheng, H., Hayden, P., Robins, A., Castro, I., 2007. Flow over cube arrays of different packing densities. Journal of Wind Engineering and Industrial Aerodynamics 95, 715–740.

Garbero, V., Salizzoni, P., Soulhac, L., 2010. Experimental study of pollutant dispersion within a network of streets. Boundary-layer meteorology 136, 457–487.

Marro, M., Gamel, H., Méjean, P., Correia, H., Soulhac, L., Salizzoni, P., 2020. High-frequency simultaneous measurements of velocity and concentration within turbulent flows in wind-tunnel experiments. Experiments in Fluids 61, 1–13.

Rafailidis, S., 1997. Influence of building areal density and roof shape on the wind characteristics above a town. Boundary-layer meteorology 85, 255–271.

Raupach, M., Hughes, D., Cleugh, H., 2006. Momentum absorption in rough-wall boundary layers with sparse roughness elements in random and clustered distributions. Boundary-Layer Meteorology 120, 201–218.

Salizzoni, P., Soulhac, L., Mejean, P., Perkins, R.J., 2008. Influence of a two-scale surface roughness on a neutral turbulent boundary layer. Boundary-layer meteorology 127, 97–110.

Tutu, N.K., Chevray, R., 1975. Cross-wire anemometry in high intensity turbulence. Journal of Fluid Mechanics 71, 785–800.